Journal of Materials Chemistry C

ROYAL SOCIETY OF CHEMISTRY

PAPER

View Article Online
View Journal

Cite this: DOI: 10.1039/d6tc00518g

Effect of aromatic ring number and substituent arrangement on the properties of phenanthro[9,10-*d*]imidazole derivatives for OLEDs

Agnieszka Krawiec,[a] Jaijanarthanan Lingagouder,[b] Agata Szlapa-Kula,[a] Michał Filapek,[a] Karol Erfurt,[c] Przemyslaw Data*[bd] and Slawomir Kula*[a]

This study investigates whether the number, arrangement, and attachment position of aromatic rings in C2 substituents influence the properties and OLED applicability of phenanthro[9,10-*d*]imidazole derivatives. We obtained ten derivatives *via* a condensation reaction, differing in only their C2 aromatic substituents: phenyl (**0A**), biphenyl-1-yl (**0B**), naphthalen-1-yl (**0C**), naphthalen-2-yl (**0D**), anthracen-9-yl (**0E**), phenanthren-9-yl (**0F**), anthracen-2-yl (**0G**), triphenylen-2-yl (**0H**), pyren-1-yl (**0I**), and perylen-3-yl (**0J**). All derivatives exhibit thermal stability above 290 °C, though this property does not directly correlate with the number of aromatic rings. Electrochemical studies showed that the redox behavior is strongly modulated by the aromatic substituent at the C2 position, with the most extended substituents exhibiting the easiest reduction; this trend is consistent with DFT results indicating substantial LUMO localization on the C2 aryl fragment. The absorption spectra of **0A–0D**, **0F**, and **0H** are largely independent of the aromatic substituent, whereas **0E**, **0G**, and **0J** show absorption features characteristic of anthracene or perylene substituents. The emission spectra of **0A–0D**, **0H**, and **0F** indicate emission from a locally-excited singlet emission state (^{1}LE), while compounds **0E**, **0G**, **0I**, and **0J** exhibit stronger substituent-dependent emission behavior. Electroluminescence studies have shown that the emission color and efficiency can be fine-tuned by changing the aromatic substituent at the C2 position. Compounds **0E**, **0I**, and **0J** combine favorable energetic parameters and strong solid-state emission, with **0J** achieving the best device performance in the series, reaching an EQE of 4.29% and a luminance of 8962 cd m^{-2}.

Received 17th February 2026,
Accepted 11th May 2026

DOI: 10.1039/d6tc00518g

rsc.li/materials-c

Introduction

Organic light-emitting diodes (OLEDs) have been generating significant interest since the groundbreaking 1987 publication by Tang and Van Slyke at Eastman Kodak.[1,2] Thanks to intensive research over the following decades, this technology has found widespread commercial applications – it is now widely used in displays, televisions, monitors, smartphones, and smartwatches.[3] The high quality of these devices is the result of the continual advancement of OLED technology, which offers numerous advantages such as low thickness and weight, flexibility, a wide color gamut, deep blacks, fast response times, and high energy efficiency.[4–6] In simple terms, OLEDs consist of a substrate, an anode, a cathode, and several functional layers: a hole transport layer (HTL), an electron transport layer (ETL), and an emission layer (EML). These individual layers can be deposited using either vacuum deposition or solution processing.[7–11] When a voltage is applied, electrostatic interactions cause the charge carriers to recombine, forming excitons – electron–hole pairs responsible for light emission.[4,12] The key components of the diode are the emitters located in the emissive layer. The greatest challenge is developing materials that emit blue light, as their key parameters – such as lifespan, stability, and color purity – still lag behind those of green and red emitters.[5,6,13–16] For this reason, research is still underway to develop new chemical compounds for use as an active layer in OLEDs. These materials must possess suitable physicochemical properties, be easy to synthesize and environmentally friendly, exhibit high purity, and show good solubility. Among the candidates tested as OLED emitters are conjugated polymers

[a] *Institute of Chemistry, Faculty of Science and Technology, University of Silesia, Szkolna 9 St., 40-007 Katowice, Poland. E-mail: slawomir.kula@us.edu.pl*
[b] *Department of Molecular Physics, Faculty of Chemistry, Lodz University of Technology, 90-543 Lodz, Poland*
[c] *Department of Organic Chemical Technology and Petrochemistry, Faculty of Chemistry, Silesian University of Technology, B. Krzywoustego 4, 44-100 Gliwice, Poland. E-mail: przemyslaw.data@p.lodz.pl*
[d] *Department of Physics, Durham University, South Road, Durham DH1 3LE, UK*

(CPs),[17–22] ionic transition metal complexes (iTMCs),[23–28] and small organic molecules (SMs).[5,6,29–35]

Phenanthro[9,10-*d*]imidazole derivatives belong to a group of small-molecule organic compounds with a complex, condensed aromatic structure. These compounds have been extensively studied as both emitters and host materials in organic light-emitting diodes (OLEDs).[5,31,32,35–70] Their rigid structure and appropriately selected energy levels enable efficient energy transfer and prevent emission quenching by limiting phenomena such as exciton quenching.[31,36,37,71] The properties of phenanthro[9,10-*d*]imidazole derivatives can be modified depending on the type of substituents in the C2 and N1 positions – electron-donating or electron-accepting groups influence the charge density distribution and thus the physicochemical properties of the system.[5,36] These derivatives are characterized by good solubility in organic solvents, high thermal stability, the ability to transport both holes and electrons, and excellent optical and electroluminescent properties.[5,31,38] This renders them a highly promising class of materials for next-generation organic optoelectronic devices.[32,35,39]

To date, numerous examples of phenanthro[9,10-*d*]imidazole derivatives have been described in the literature for use in OLEDs.[5,31,32,35–70] In the structural aspect, the considered compounds differ in terms of substituents, in particular in the C2 position.[5,31,32,36–66] Despite numerous studies, it remains difficult to determine which substituents or structural modifications are most beneficial for OLED applications. Therefore, we attempted to systematically vary the substituents at the C2 position in phenanthro[9,10-*d*]imidazole derivatives to elucidate the dynamics of their property changes. Therefore, in this article, we examined the effect of the number of aromatic rings in the substituent of phenanthro[9,10-*d*]imidazole derivatives on their thermal, electrochemical, and optical properties, as well as their potential for OLED applications. Furthermore, during our studies, we considered the arrangement of the aromatic rings and the position of the substituent attachment to the molecular core. To better determine the effect of the aromatic rings at the C2 position, we omitted the substituent at the N1 position (leaving the N–H group unsubstituted). The studies were carried out on ten phenanthro[9,10-*d*]imidazole derivatives for which the number of aromatic rings and their arrangement at the C2 substituent changed progressively in the following order: phenyl (**0A**), biphenyl-1-yl (**0B**), naphthalen-1-yl (**0C**), naphthalen-2-yl (**0D**), anthracen-9-yl (**0E**), phenanthren-9-yl (**0F**), anthracen-2-yl (**0G**), triphenylen-2-yl (**0H**), pyren-1-yl (**0I**), and perylen-3-yl (**0J**). Finally, organic light-emitting diodes containing derivatives **0A–0J** were constructed, and their parameters were determined. The experimental studies were supplemented with theoretical considerations based on DFT calculations.

Experimental section

All details concerning the chemicals, materials, apparatus, experimental procedures, DFT calculations, and device characterization are provided in the SI. The SI also includes NMR and HRMS spectra, TGA thermograms, voltammograms, absorption, and emission spectra of the compounds.

Results and discussion

Synthesis and thermal characterization

All phenanthro[9,10-*d*]imidazole derivatives (**0A–0J**) were obtained by a series of condensations involving the reaction of 9,10-phenanthrenedione with aromatic aldehydes varying in the number of aromatic rings and their substitution position (Fig. 1). The syntheses were carried out with ammonium acetate and acetic acid. The reaction conditions involved heating the reaction mixtures at reflux for 24 hours under argon. The crude products of the obtained phenanthro[9,10-*d*]imidazole derivatives were precipitated by adding water to the reaction mixtures. The resulting precipitates were filtered and thoroughly washed with water to remove residual ammonium acetate and acetic acid. Finally, the synthesized compounds were crystallized twice in methanol. The chemical structures of the **0A–0J** derivatives were confirmed by NMR spectroscopy and HRMS (Section 4). The syntheses gave ten phenanthro[9,10-*d*]imidazole derivatives in yields ranging from 23% to 95%. It is worth noting that the procedure employed is straightforward and efficient. The derivatives under consideration can be purified

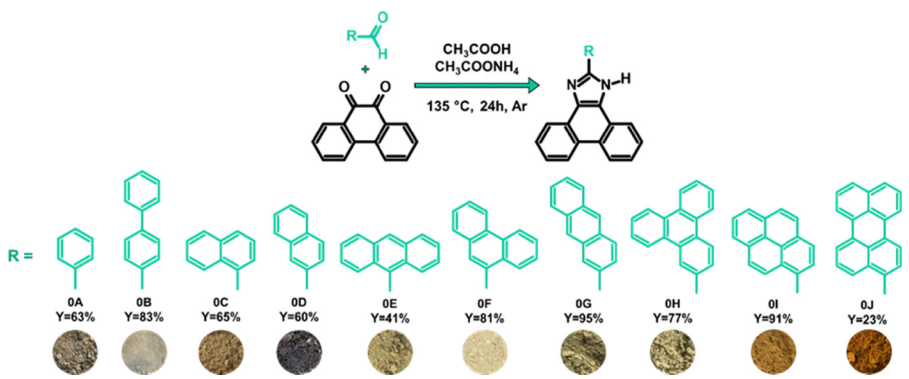

Fig. 1 Synthesis of phenanthro[9,10-*d*]imidazole derivatives (**0A–0J**) with yields and photographs of precipitates.

by crystallization, and their structures were confirmed using standard methods for organic compounds.

Thermal properties are a crucial step in evaluating organic compounds for potential use in modern electronic devices. During the operation of devices such as laptops and smartphones, the temperature of their components can rise significantly. Therefore, chemical compounds that could be used as light emitters must exhibit high thermal stability. Adequate thermal resistance of the material is crucial for maintaining long-term performance and device reliability. Low thermal stability of the materials used can lead to degradation of the molecular structure, reduced light emission efficiency, and even permanent damage to the device.[72–75] Determining basic thermal parameters enables the assessment of compounds' resistance to elevated temperatures and thus allows predicting their behavior under real operating conditions of electronic devices.

Thermogravimetric analysis (TGA) was used to assess the thermal stability of the tested derivatives, which allowed us to determine the temperatures of 5% and 10% mass loss (T_5 and T_{10}) and the decomposition temperature (T_d). In addition, the melting temperatures (T_m) and glass transition temperatures (T_g) were determined using differential scanning calorimetry (DSC). The obtained results are summarized in Table 1. Phenanthro[9,10-*d*]imidazole derivatives generally exhibit high thermal stability, which results from the presence of a condensed aromatic core.[31,32,39–46,48,50–53,55–59,61,64–66] In the case of **0A–0J**, the 5% weight loss occurs in the range of 292–363 °C. Compound **0B**, having a biphenyl-1-yl substituent, is characterized by a surprisingly high stability of 337 °C compared to **0A**, **0C**, and **0D**. Comparing derivatives bearing a tricyclic aromatic substituent at the C2 position (for **0E** anthracen-9-yl, for **0F** phenanthren-9-yl, and for **0G** anthracen-2-yl), we observe the same 5% weight loss for **0F** and **0G** at 313 °C, while for **0E** it is higher by 14 °C. In turn, derivatives **0H** and **0I**, having a triphenylene-2-yl and pyren-1-yl substituent, are characterized by the highest thermal stability of 363 °C and 362 °C, respectively. Compound **0J** with a perylene-3-yl substituent exhibits a T_5 of 317 °C, which is similar to that observed for compounds **0D**, **0F**, and **0G**. The temperature range of 10% mass loss (T_{10}) for the analyzed derivatives is between 305 °C and 385 °C, while decomposition temperatures (T_d) exceed 365 °C. Melting point (T_m) is observed in the range of 228–321 °C; the exceptions are compounds **0A**, **0E**, and **0F**, for which no melting process was observed. The glass transition temperatures (T_g) were determined for **0B**, **0C**, **0D**, **0G**, **0I**, and **0J**. They were in the range of 115–172 °C. No clear upward trend in thermal stability is observed with increasing the number of aromatic rings in the C2 substituent of phenanthro[9,10-*d*]imidazole. However, all analyzed derivatives remain stable above 292 °C, which is an important parameter guaranteeing reliable operation of the materials under conditions typical of electronic devices. Thermograms and DSC are presented in SI (Fig. S1–S7).

Table 1 Thermal parameters of **0A–0J**

Compound	T_5[a] [°C]	T_{10}[b] [°C]	T_{max}[c] [°C]	T_m[d] [°C]	T_g[e] [°C]
0A	292	305	365	—	—
0B	337	352	407	270	121
0C	308	327	396	228	125
0D	314	341	408	248	115
0E	327	345	412	—	—
0F	313	354	428	—	—
0G	313	340	395	271	122
0H	363	385	441	298	—
0I	362	379	422	318	146
0J	317	371	476	321	172

[a] T_5 – 5% weight loss temperature. [b] T_{10} – 10% weight loss temperature. [c] T_d – temperature of maximum decomposition rate. [d] T_m – melting point. [e] T_g – glass transition temperature.

Redox behavior

The next stage of the research involved a series of measurements using cyclic voltammetry (CV), which is employed to study the electrochemical properties of dissolved compounds. CV measures the electric current flowing through the electrochemical system in response to a linearly changing potential of the working electrode. These measurements allow the determination of ionization potential (IP), electron affinity (EA), and energy gap (E_g) of the investigated compounds (assuming the IP of ferrocene equals −5.1 eV).[76] This, in turn, allows us to calculate the energy band gap (E_g), which is the key value. The IP value was determined from the oxidation peak onset (by extrapolating the linear peak fragment to the background line), and the EA potential was similarly determined for the reduction peak. Representative voltammograms showing the redox behavior of the compounds are shown below (Fig. 2). All reduction and oxidation voltammograms obtained during the research are presented in the SI (Fig. S8 and S9). In addition, a summary table describing the electrochemical and optical parameters is provided below (Table 2).

As already mentioned, blue-emitting organic compounds are intensively researched due to their wide range of applications,

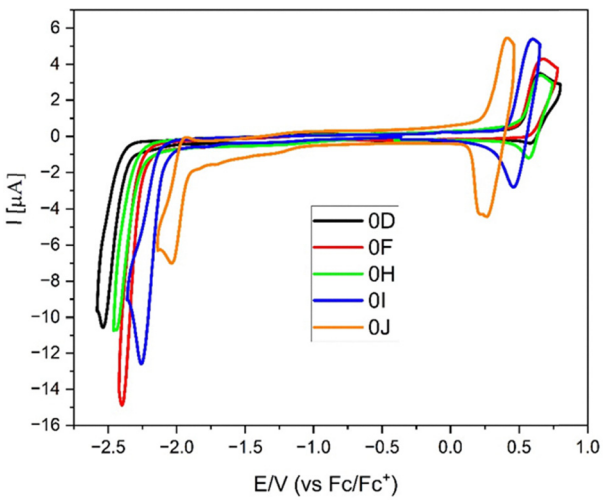

Fig. 2 Cyclic voltammograms of the investigated compounds with sweep rate ν = 100 mV s^{-1}, 0.1 M Bu_4NPF_6 in CH_2Cl_2 (c = 1 × 10^{-3} mol L^{-1}).

Table 2 Electrochemical properties of **0A–0J**

Compound	E_{1red} [V]	E_{1ox} [V]	EA[a] [eV]	IP[b] [eV]	$E_{g(CV)}$[c] [eV]	λ_{onset} [nm]	$E_{g(opt)}$[d] [eV]
0A	−2.25	0.53	−2.85	−5.63	2.78	376	3.30
0B	−2.25	0.50	−2.85	−5.60	2.75	388	3.20
0C	−2.41	0.50	−2.69	−5.60	2.91	390	3.18
0D	−2.33	0.51	−2.77	−5.61	2.84	400	3.10
0E	−2.03	0.45	−3.07	−5.55	2.48	424	2.92
0F	−2.22	0.50	−2.88	−5.60	2.72	391	3.17
0G	−2.14	0.39	−2.96	−5.49	2.53	430	2.88
0H	−2.25	0.51	−2.85	−5.61	2.76	396	3.13
0I	−2.10	0.41	−3.00	−5.51	2.51	433	2.86
0J	−1.89	0.26	−3.21	−5.36	2.15	502	2.47

[a] Calculated from CV measurements: EA = −5.1 − E_{red}. [b] Calculated from CV measurements: IP = −5.1 − E_{ox}. [c] Calculated from CV measurements: $E_{g(CV)} = E_{ox(onset)} - E_{red(onset)}$. [d] Obtained from UV-vis using $E_g = 1240/\lambda_{onset}$ formula.

including biomedical applications, photolithography, and (above all) OLEDs. In the case of OLEDs, one of the most promising compound groups is phenanthro[9,10-*d*]imidazole derivatives.[77] To check whether the tested compounds exhibit appropriate energetic parameters and redox stability, tests in diluted solutions are extremely useful. First, the electrochemical properties during negative potential sweeping were investigated. As expected, for most derivatives, reduction occurs when the external potential is below −2 volts, which is consistent with the results for other phenanthro[9,10-*d*]imidazole compounds.[78–80] The influence of the substituent at position C2 is quite clearly visible. In the case of systems with a longer conjugated system (**0E**, **0G**, **0I**), reduction occurs more easily (between −2.03 V and −2.14 V) than for molecules with fewer fused rings (for which E_{red} is below −2.25 V). A special case is the derivative **0J** for which the reduction occurs most easily (−1.89 V), and the process is thermodynamically reversible. It can therefore be assumed that for this compound, the electron is accepted by the perylene substituent. Therefore, the strong influence of the R substituent on both the magnitude and nature of the reduction suggests that it occurs mainly on this substituent. This observation was confirmed by DFT calculations, where for each molecule the LUMO orbital lies mainly (or almost exclusively) on the aromatic rings at the C2 position. Similar patterns were observed for the oxidation, *i.e.*, all of the derivatives with small substituents undergo this process above 0.5 V. Derivatives **0E**, **0G**, and **0I** again show an intermediate character, while oxidation occurs most easily for derivative **0J**. Importantly, in the case of oxidation, several compounds exhibited reversible thermodynamic behavior of this process, which is particularly valuable due to its potential applications in OLED technology.

Considering the redox parameters, the electrochemical energy gap can be calculated. Since this parameter results directly from E_{red} and E_{ox}, there is a clear difference between the four compounds (namely: **0E**, **0G**, **0I**, **0J**) having E_g in the range of 2.15 to 2.53 eV and the remaining derivatives (E_g above 2.72 eV). This agrees very well with the UV-vis absorption spectroscopy tests' results, where the λ_{onset} is above 400 nm for the four above-mentioned molecules, and for the remaining compounds, below this value. Regarding the energy gap values, it is clear that optically determined band gaps are overestimated relative to electrochemical ones, which is a common phenomenon. When comparing the exact values of experimentally determined energy gaps, it is important to remember their specificity. The electrochemical method delivers or withdraws an electron to or from the molecule. Absorption, on the other hand, excites and transfers an electron within the molecule. Therefore, in the case of complex systems with separated frontier orbitals, the optical gap is always larger than the electrochemical gap. Considering the redox stability of the tested derivatives, several spectroelectrochemical measurements were conducted. This experiment is possible only for compounds having stable (non-degradable) oxidized and/or reduced forms. As shown in Fig. 3a, in the case of oxidation of compound **0H**, the initial band between 320 and 400 nm starts to disappear, while a broad band from 400 to 575 nm appears and grows. This means that this process takes place

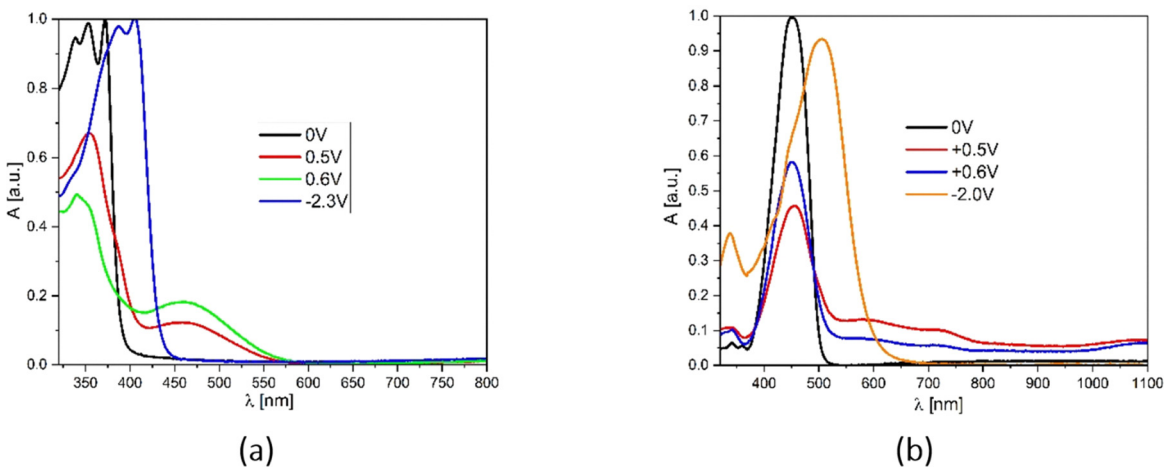

Fig. 3 (a) UV-Vis spectroelectrochemistry of the **0H** and (b) **0J** derivative in CH_2Cl_2 solution ($c = 1 \times 10^{-4}$ mol L^{-1}, as an inset on the graph potentials *vs.* Fc/Fc^+ redox couple).

within the molecule fragment that is responsible for the color of the molecule, *i.e.*, the lowest energy electronic transition. In the case of reduction, the entire original band shifts by 50 nm towards higher wavelengths but retains (approximately) its shape. This suggests that the nature of the main electronic transition remains unchanged (electrons are excited from the same fragment of the molecule), and that the additional electron injected from the electrode is localized near this moiety. Similar behavior was observed for the **0J** derivative (Fig. 3b). Also, in this case, exceeding the oxidation potential causes the disappearance of the output band. However, for this derivative, the band that appears is much broader, covering the entire available spectral range (up to 1100 nm), which is characteristic of p-doping molecules with a system of several alternating double and single bonds. Therefore, this process must (at least in part) involve a perylene substituent. In turn, reduction (similarly to **0H**) causes a shift of the entire band towards higher wavelengths (by about 100 nm) but also causes its broadening.

DFT calculations

To better understand the electronic properties of synthesized compounds **0A–0J**, density functional theory (DFT) calculations were performed with the PBE0 functional[81,82] in conjugation with the def2TZVP basis set.[83–88] Furthermore, it was verified that the vibrational spectra did not contain imaginary frequencies and that the optimized structures were at a minimum point on the potential energy surface. The optimized ground-state geometries were used to calculate electronic absorption spectra using the time-dependent DFT (TDDFT) formalism at the PBE0/def2TZVP level of theory. The experimental CH_2Cl_2 solution was mimicked using a polarizable continuum model to obtain UV-vis absorption spectra.[89,90] According to DFT calculations, some of the studied compounds adopt nonplanar geometry. This applies to the dihedral angle between the plane of the aromatic group and the central 1*H*-phenanthro[9,10-*d*]imidazole core (Fig. S10). The nonplanarity of these molecules results from steric hindrance between the peripheral hydrogen atoms of the substituent and the core. Replacing the 1-naphthalene (**0C**) and 9-anthracene (**0E**) substituents with 2-naphthalene (**0D**) and 2-anthracene (**0G**) leads to complete planarization of the molecule. The **0E** compound exhibits the largest torsion angle. The larger the torsion angle, the smaller the delocalization of π electrons between the aryl substituent and the 1*H*-phenanthro[9,10-*d*]imidazole core in the ground state.[91] Analyzing the orbital distribution in the presented group, it can be observed that the molecules do not exhibit well-separated distributions of the highest occupied molecular orbital (HOMO) and the lowest unoccupied molecular orbital (LUMO). In the case of the HOMO, it is located throughout the molecule. For **0B**, **0D**, **0F**, and **0H**, this orbital is situated to a greater extent on the 1*H*-phenanthro[9,10-*d*]imidazole core (Table 3). Interestingly, **0J** is an exception, where the HOMO orbital is located more on the substituent, as well as on the imidazole ring. The LUMO orbital primarily encompasses substituents in the C2 position. The exception is molecule **0A**, which fully distributes this orbital throughout the molecule. The values of the frontier orbitals are presented in Table 4.

For optoelectronic materials, determining charge injection is a key element in assessing luminance performance. The ionization potential and electron affinity of molecules are the most important parameters characterizing their ability to inject holes and electrons, respectively.[92,93] To evaluate the energy barriers for injecting holes and electrons from electrodes into organic material molecules serving as emission or charge transport layers in the devices, respectively, the IP and EA, both vertical (v, in the neutral molecule geometry) and adiabatic (a, optimized structure for both neutral and charged molecules), reorganization energies (λ), and hole extraction potential (HEP) and electron extraction potential (EEP) were calculated. HEP is the energy difference between M^+ (cationic) and M_0 (neutral molecule) using the M^+ geometric structure, and EEP is the energy difference between M^- (anionic) and M_0 using the M^- geometric structure in the calculations.[92,93] In connection with the above, ionization potentials (IP) and electron affinities (EA) were calculated for all 1*H*-phenanthro[9,10-*d*]imidazole derivatives (Table 4 and S1). These values more closely correspond to those obtained from electrochemical measurements. IP energies range from 5.25 eV to 5.61 eV. The presented data indicate that compounds **0E**, **0G**, **0I**, and **0J** undergo oxidation most readily. For EA, the energy range is from 1.76 eV to 2.69 eV. Interestingly, compounds with less negative IP values, indicating ease of oxidation, exhibit the opposite trend in EA and reduction. As can be observed, the energy values of the HOMO orbital are closer to the IP value than the LUMO values are to the EA. The energy gap resulting from the difference between IP and EA is 2.57–3.86 eV.

The derivative with a perylene substituent has the most favorable gap. As is known, achieving high EA_v and low IP_v values of emitters is crucial for improving the electroluminescence efficiency of OLEDs.[93] This rule is satisfied by the values obtained for the **0J** compound (Table S1), which turned out to be the best among the tested OLEDs. Analyzing the data obtained for **0H** and **0F**, it can be concluded that both compounds are more similar to less electron-rich molecules.

As shown in Table S1, the λ_{hole} values for the **0A–0H** series are lower than those obtained for the $\lambda_{electron}$. Therefore, hole transfer in the molecules is more efficient than electron transfer. Furthermore, with increasing the number of aromatic rings in the C2 substituent, the difference between λ_{hole} and $\lambda_{electron}$ decreases. The exception is **0A**, for which the difference is 0.10 eV. A small value of $\Delta\lambda$ indicates that these molecules exhibit a better balance between hole and electron transport. Comparing the compounds in the **0C–0D** and **0E–0G** pairs, one can observe a dependence of the dihedral angle on the λ_{hole} and $\lambda_{electron}$ values. The smaller the torsion angle, the smaller the values of hole and electron reorganization. Absorption spectra were calculated using the TD-DFT method to better understand the optical properties. As can be seen in Fig. S11, the theoretical spectra correlate well with the experimental results.

The measured bands in the 300–350 nm range associated with π–π* transitions originating from the 1*H*-phenanthro[9,10-*d*]imidazole fragment correspond to the HOMO → LUMO

Table 3 Collected data on photophysical properties of **0A–0J**

Compound	HOMO	LUMO	Compound	HOMO	LUMO
0A	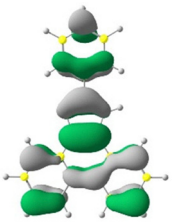	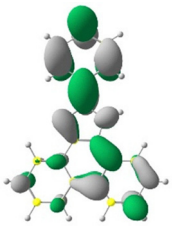	**0F**	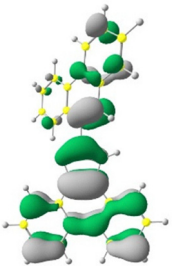	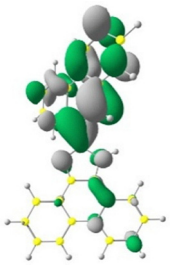
0B	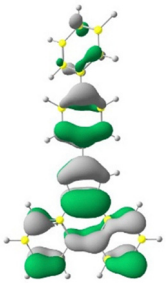	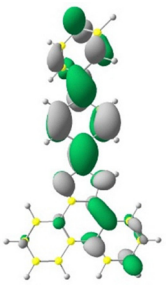	**0G**	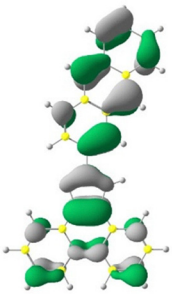	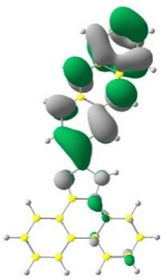
0C	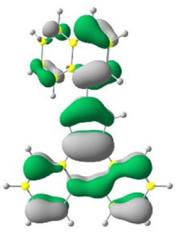	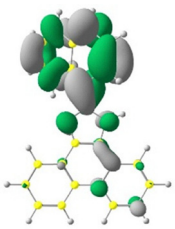	**0H**	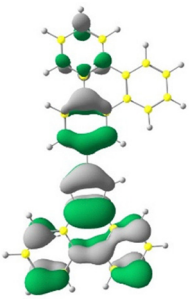	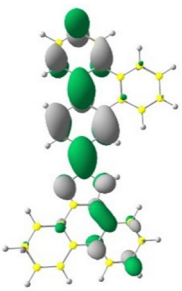
0D	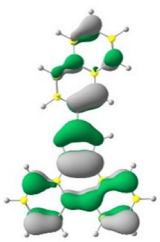	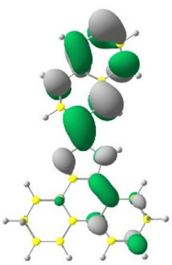	**0I**	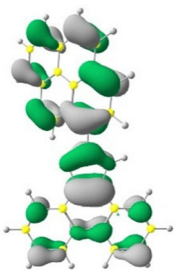	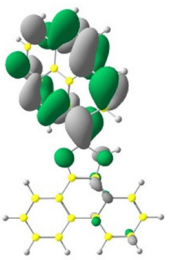
0E	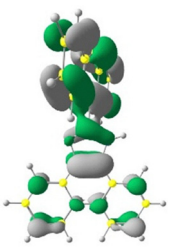	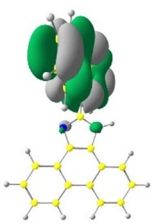	**0J**	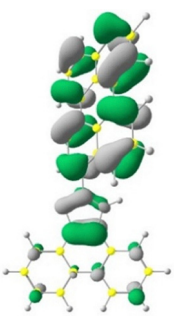	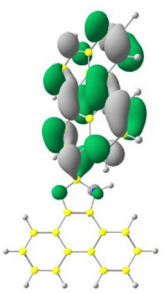

transition. For compounds with the lowest energy absorption bands above 350 nm, these bands also correspond to the HOMO → LUMO transition. The theoretical optical gap was calculated from the simulated absorption spectra. This gap was in the range of 2.25–3.43 eV. The lowest optical gap was characterized by compound **0J** (Table 4). Natural transition orbital (NTO) calculations were performed for all the presented molecules. This enabled characterization of the excited states. As shown in Fig. S12, the **0A–0J** derivatives can be divided into two groups. The first group exhibits a predominantly LE

Table 4 Data obtained from DFT calculations

Compound	Dihedral angle[a] (°)	$HOMO_{(DFT)}$ [eV]	$LUMO_{(DFT)}$ [eV]	$IP_{(DFT)}$ [eV]	$EA_{(DFT)}$ [eV]	$E_{g(DFT)}$ [eV]	$IP–EA_{(DFT)}$ [eV]	$E_{g(opt\ DFT)}$ [eV]
0A	0	−5.86	−1.45	5.61	1.76	4.40	3.86	3.38
0B	15.32	−5.80	−1.67	5.55	2.02	4.13	3.54	3.15
0C	37.18	−5.85	−1.68	5.58	2.07	4.16	3.51	3.16
0D	0	−5.82	−1.74	5.57	2.03	4.08	3.55	3.13
0E	65.26	−5.80	−2.14	5.48	2.43	3.66	3.05	2.71
0F	38.69	−5.86	−1.72	5.59	2.12	4.14	3.47	3.15
0G	0	−5.68	−2.17	5.46	2.43	3.50	3.04	2.64
0H	3.86	−5.80	−1.78	5.56	2.07	4.03	3.50	3.06
0I	34.46	−5.68	−2.06	5.42	2.36	3.62	3.07	2.75
0J	42.40	−5.49	−2.42	5.25	2.69	3.07	2.57	2.23

[a] The angle between the phenanthro[9,10-*d*]imidazole and the substituent.

character (see the $S_0 \rightarrow S_1$ transition), due to the large overlap of ''holes'' and ''particles'' in the NTO. The second group comprises compounds **0E**, **0G**, **0I**, and **0J**. They are characterized by a noticeable spatial separation between the ''hole'' and ''particle'' wave functions, but also exhibit partial overlap. This indicates the hybridized local and charge-transfer (HLCT) character of these compounds.[94–96]

Optical properties

With the derivatives **0A–0J** in hand, we set out to investigate their absorption and emission spectra in different solvents. The selection was made based on the nonpolar, polar aprotic, and polar protic nature of solvents such as toluene, chloroform ($CHCl_3$), tetrahydrofuran (THF), acetonitrile (MeCN), dimethyl sulfoxide (DMSO), and methanol (MeOH). The studies were performed in solutions with a concentration of 1×10^{-5} mol L^{-1}, where the probability of intermolecular π–π stacking interaction is negligible. All results and the necessary spectra are presented in Table 5 and Fig. S13 in the SI. The absorption profiles and the position of the maximum absorption band of all tested molecules **0A–0J** remain almost unchanged with increasing solvent polarity, which indicates the absence of solvatochromism. Therefore, it can be concluded that the HOMO–LUMO gaps for **0A–0J** are the same in all tested solvents, because solvatochromism depends on the degree of charge separation in the ground state of the chromophore.[97] Moreover, it can be concluded that the ground-state dipole characteristics are similar in low- and high-polarity solvents. This is because increasing solvent polarity does not cause significant changes in the absorption spectra of the presented compounds.[98]

Analyzing the obtained spectra, it is clear that these compounds have peaks located in the UV (**0A–0F** and **0H–0I**) and UV-vis (**0G** and **0J**) ranges. All derivatives' bands in the 300–350 nm range are associated with π–π* transitions originating from the 1*H*-phenanthro[9,10-*d*]imidazole core.[99] The absorption spectra of **0A–0D**, **0F**, and **0H** are rather insensitive to the attached aryl group (at the C2 position) over the entire spectral range. Comparing the shapes of these spectra to the results reported in the literature for 1*H*-phenanthro[9,10-*d*]imidazole reveals a substantial similarity.[99] The introduction of aromatic substituents at the C2 position leads only to a substantial increase in the extinction coefficient, which also indicates the π–π* character (Fig. 4a).[99] In the case of **0I**, the shape of the absorption spectrum does not resemble that of the core molecule itself. However, the low-energy absorption band (∼380 nm) can also be attributed to the delocalized π–π* transition of 1*H*-phenanthro[9,10-*d*]imidazole. This is confirmed by literature reports of structurally similar compounds.[100,101]

As reported in the literature, a red shift in absorption and emission is observed with increasing aryl group size. This shows that the optical band gap decreases with increasing π-electron coupling.[102] The same dependence was observed in the **0A–0J** series (Tables 2 and 3). Furthermore, the structural parameter controlling the π-system overlap in aryl rings is the torsion angle.[103] Planar structures with torsion angles ∼0° are expected to have maximum π-system overlap and, as a result, small optical gap values, whereas structures with torsion angles close to 90° should have large optical gap values.[103] Therefore, the dependence of the dihedral angle on the values of the obtained optical gaps was investigated (Fig. 5). Analyzing the correlation between the optical gap and the dihedral angle across the group, a large scatter in the point positions is observed, with a weak trend (Fig. 5). Generally, a tendency is observed towards a decrease in the optical gap associated with an increase in the number of rings in the C2 substituent. The exceptions are compounds **0F** and **0H**, which have optical gaps close to those of compounds **0A–0D**. Interestingly, when comparing compounds in the **0C–0D** and **0E–0G** pairs (with the same number of rings), this relationship is noticeable. Compounds with 0° of torsion (**0D** and **0G**) have a smaller experimental and theoretical optical gap than their **0C** and **0E** counterparts with a torsion angle greater than 35°.

The situation changes for **0E** and **0G**, where the bands in the 350–450 nm range exhibit spectral features typical of the ^{1}π–π* anthracene absorption.[91] **0E** and **0G** exhibiting a bathochromic shift relative to anthracene itself. The absorption band with $\lambda_{max} \sim 450$ nm for **0J** corresponds to the 3-perylene substituent, respectively. Interestingly, compared to free perylene, it is noticeably broadened and bathochromically shifted. This may indicate some π delocalization from electron-rich perylene to the acceptor unit of the 1*H*-phenanthro[9,10-*d*]imidazole core.[91] An essential aspect of the study is evaluating the effect of the substituent on optical properties. Molecules **0A**, **0C**, and **0F** are the most hypsochromically shifted. **0J** is the most

Table 5 Collected data on photophysical properties of **0A–0J**

Compound	Solvent	ε [10^4 dm^3 mol^{-1} cm^{-1}]	λ_{abs} [nm]	λ_{em} [nm]	Stokes shift[a] [nm]	Stokes shift[a] [cm^{-1}]	QY	QY_{AE}
0A	Toluene	2.48, 2.91, 3.12, 1.98, 1.70	288, 317, 331, 347, 365	376, 394	11	802	0.18	0.23
	$CHCl_3$	1.75, 2.23, 2.20, 1.33, 1.12	286, 316, 328, 351, 363	380, 394	17	1232	0.08	0.15
	THF	2.26, 2.96, 3.03, 1.71, 1.53	286, 316, 330, 350, 363	376, 391	13	952	0.21	0.33
	MeCN	1.93, 2.73, 2.69, 1.36, 1.18	286, 314, 324, 346, 362	377, 388	15	1099	0.15	0.29
	DMSO	1.42, 2.13, 2.11, 1.21, 1.08	288, 316, 329, 350, 364	380, 391	16	1157	0.24	0.33
	MeOH	1.61, 2.16, 1.93, 1.11, 1.06	286, 310, 323, 343, 358	370, 385	12	906	0.19	0.32
	Solid	—	—	427, 448	—	—	—	—
0B	Toluene	2.61, 2.55, 2.46	340, 352, 371	391, 410	20	1379	0.36	0.42
	$CHCl_3$	3.08, 2.93, 2.61	339, 350, 369	411	42	2769	0.25	0.30
	THF	3.00, 2.73, 2.74	340, 353, 372	406	34	2251	0.45	0.49
	MeCN	4.17, 3.54, 3.38	337, 350, 368	408	40	2664	0.41	0.52
	DMSO	3.39, 3.60, 3.64	341, 353, 374	416	42	2700	0.46	0.47
	MeOH	4.06, 3.47, 3.16	334, 346, 365	403	38	2583	0.51	0.54
	Solid	—	—	435, 457, 493	—	—	—	—
0C	Toluene	1.37, 1.07, 1.18, 1.24	286, 311, 346, 363	402, 421	39	2673	0.22	0.24
	$CHCl_3$	1.89, 1.66, 1.65, 1.37	284, 308, 330, 360	429	69	4468	0.12	0.17
	THF	1.53, 1.34, 1.51, 1.50, 1.40	286, 309, 336, 346, 365	418	53	3474	0.31	0.32
	MeCN	1.34, 1.36, 1.46, 1.22	284, 308, 331, 360	423	63	4137	0.26	0.38
	DMSO	1.59, 1.43, 1.51, 1.50, 1.47	285, 312, 338, 346, 366	428	62	3958	0.29	0.30
	MeOH	2.24, 2.27, 1.92, 1.55, 1.37	286, 304, 322, 340, 356	417	61	4109	0.24	0.39
	Solid	—	—	430, 450	—	—	—	—
0D	Toluene	3.27, 1.96, 3.23, 3.27, 3.78	293, 309, 340, 354, 373	386, 404	13	903	0.30	0.34
	$CHCl_3$	2.13, 1.56, 2.24, 2.26, 2.19	290, 309, 337, 353, 371	402	31	2079	0.19	0.24
	THF	3.17, 2.18, 3.43, 3.27, 3.98	289, 312, 339, 353, 372	401	29	1944	0.46	0.47
	MeCN	2.28, 2.27, 2.78, 2.39, 2.64	289, 323, 335, 352, 368	404	36	2421	0.34	0.49
	DMSO	3.70, 3.45, 4.23, 3.91, 4.66	289, 327, 340, 356, 373	410	37	2419	0.35	0.41
	MeOH	2.34, 2.02, 2.68, 2.33, 2.44	286, 309, 333, 347, 366	398	32	2197	0.42	0.49
	Solid	—	—	432, 453	—	—	—	—
0E	Toluene	9.8, 6.1, 3.9, 6.3, 6.8	286, 306, 348, 368, 386	497	111	5786	0.12	0.13
	$CHCl_3$	9.8, 6.5, 4.8, 6.9, 7.1	286, 305, 350, 369, 387	503	116	5959	0.08	0.23
	THF	9.0, 5.7, 3.8, 5.9, 6.2	286, 307, 346, 365, 385	485	100	5355	0.22	0.24
	MeCN	9.8, 10.0, 3.1, 4.8, 4.9	287, 299, 346, 365, 383	490	107	5701	0.15	0.27
	DMSO	9.9, 5.6, 3.9, 5.9, 6.1	286, 308, 351, 369, 388	494	106	5530	0.19	0.29
	MeOH	9.9, 7.1, 6.0, 8.5, 8.0	286, 301, 347, 364, 383	470	87	4833	0.23	0.31
	Solid	—	—	512	—	—	—	—
0F	Toluene	1.80, 2.02, 2.06, 1.95	307, 336, 346, 364	406, 424	42	2842	0.24	0.33
	$CHCl_3$	1.17, 1.66, 1.32	304, 332, 361	428	67	4336	0.15	0.20
	THF	1.62, 1.91, 1.89, 1.78	309, 336, 348, 365	419	54	3531	0.25	0.39
	MeCN	1.60, 1.88, 1.75, 1.62	309, 333, 345, 363	427	64	4129	0.30	0.48
	DMSO	1.77, 1.91, 1.89, 1.84	309, 337, 349, 366	433	67	4228	0.30	0.34
	MeOH	1.65, 1.48, 1.23, 1.05	303, 324, 341, 357	418	61	4088	0.31	0.32
	Solid	—	—	439	—	—	—	—
0G	Toluene	2.23, 3.17, 1.48, 1.53, 1.47	327, 342, 367, 392, 415	446	31	1674	0.22	0.29
	$CHCl_3$	2.64, 3.41, 1.63, 1.66, 1.50	326, 340, 366, 388, 410	455	45	2412	0.38	0.39
	THF	2.13, 2.88, 1.34, 1.44, 1.31	324, 399, 367, 385, 405	453	48	2616	0.37	0.54
	MeCN	2.31, 2.90, 1.34, 1.48, 1.28	323, 334, 364, 382, 402	471	69	3644	0.28	0.44
	DMSO	2.45, 3.20, 1.57, 1.63, 1.49	328, 340, 368, 388, 409	484	75	3789	0.27	0.30
	MeOH	2.98, 1.48, 1.55, 1.26	333, 360, 381, 399	459	60	3276	0.34	0.35
	Solid	—	—	481	—	—	—	—
0H	Toluene	1.42, 2.94, 3.49, 4.05	313, 346, 364, 382	398, 418	16	1052	0.39	0.44
	$CHCl_3$	1.65, 3.10, 3.45, 3.50	341, 344, 361, 379	402, 418	23	1510	0.24	0.35
	THF	1.49, 3.01, 3.30, 3.82	312, 344, 359, 379	397, 411	18	1196	0.44	0.55
	MeCN	1.68, 3.33, 3.49, 3.80	311, 340, 357, 375	414	39	2512	0.45	0.56
	DMSO	1.58, 3.10, 3.50, 3.96	315, 345, 362, 379	419	40	2519	0.46	0.46
	MeOH	1.81, 3.29, 3.34, 3.30	310, 339, 355, 373	410	37	2419	0.52	0.53
	Solid	—	—	457	—	—	—	—
0I	Toluene	1.46, 2.92	312, 383	439, 464	56	3330	0.28	0.32
	$CHCl_3$	1.40, 2.74	310, 380	446, 463	66	3894	0.27	0.35
	THF	1.43, 3.04	309, 380	449	69	4044	0.36	0.40
	MeCN	1.98, 4.16	307, 378	465	87	4949	0.31	0.37
	DMSO	2.27, 4.33	310, 384	472	88	4855	0.32	0.34
	MeOH	2.12, 1.19, 3.07, 3.84	305, 327, 343, 366	454	88	5296	0.29	0.33
	Solid	—	—	472	—	—	—	—
0J	Toluene	0.86, 0.52, 0.46, 3.08	310, 347, 368, 454	506, 539	52	2264	0.32	0.33
	$CHCl_3$	0.87, 0.48, 0.41, 3.33	309, 345, 367, 450	505, 539	55	2420	0.33	0.38
	THF	0.82, 0.48, 0.42, 2.85	308, 346, 367, 454	505, 536	51	2224	0.31	0.34
	MeCN	0.88, 0.58, 0.55, 3.36	304, 346, 365, 452	504, 529	52	2283	0.34	0.45
	DMSO	0.87, 0.48, 0.41, 3.30	309, 348, 369, 460	515, 542	55	2322	0.35	0.36
	MeOH	0.92, 0.47, 0.46, 3.48	302, 342, 358, 443	498, 527	55	2493	0.40	0.41
	Solid	—	—	548	—	—	—	—

[a] $\lambda_{em} - \lambda_{abs}$.

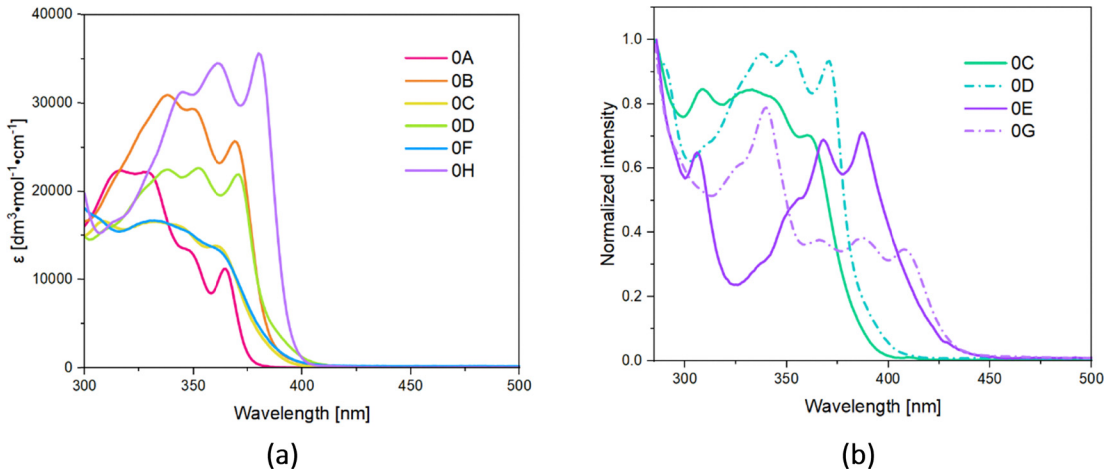

Fig. 4 (a) Absorption spectra of compounds **0A–0D**, **0F** and **0H** in $CHCl_3$ and (b) bathochromic shift observed in pairs **0C–0D** and **0E–0G** ($c = 1 \times 10^{-5}$ mol L^{-1}).

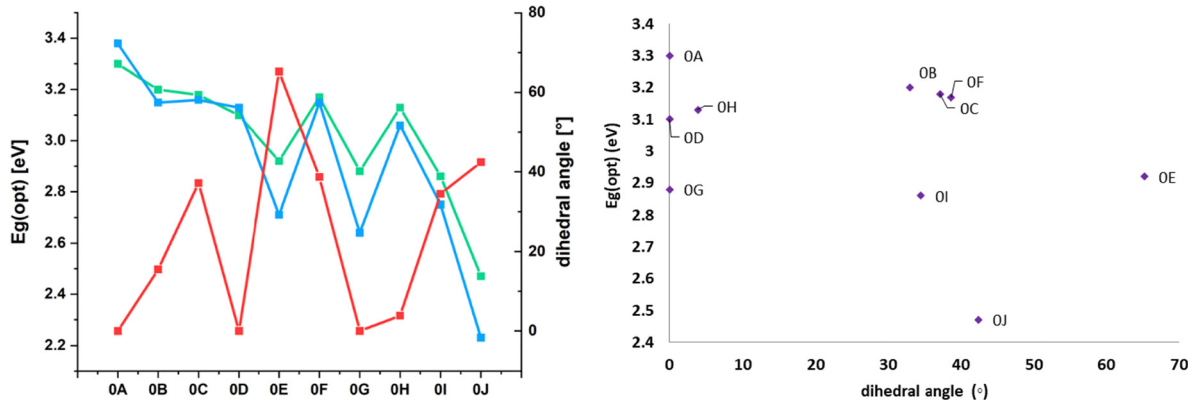

Fig. 5 Dependence of the dihedral angle (red line) on the optical (green line) and theoretical (blue line) gap energy, along with the point spread.

red-shifted. A bathochromic shift is also observed when comparing derivatives in the **0C–0D** and **0E–0G** pairs. Replacing the 1-naphthalene (**0C**) and 9-anthracene (**0E**) substituents with 2-naphthalene (**0D**) and 2-anthracene (**0G**) substituents results in a red shift due to the greater planarity of the molecule and better coupling between the substituent and the core (Fig. 4b and S14).

In the next step, the behavior of the molecules in emission measurements was examined. The emission maxima of the compounds, depending on the substituent and solvent polarity, range from 370 to 542 nm. Molecule **0A** exhibits a vibronic structure in all solvents presented (Fig. S13). This is consistent with literature reports for this molecule.[99] In toluene, the fluorescence spectra of **0B–0D**, **0H**, and **0F** also have well-defined vibronic structures and resemble the emission profile of **0A**, however, they are more bathochromically shifted relative to it. The well-structured fluorescence band indicates emission from a locally-excited singlet emission state (^{1}LE). Changing to a more polar solvent causes the disappearance of the vibronic structure in the case of **0B–0D**, **0H**, and **0F**. This supports the concept that in a more extended system, upon excitation, the 1*H*-phenanthro[9,10-*d*]imidazole moiety may undergo partial planarization (or solvent rearrangement) with the aryl ring of the substituent.[99] In compounds **0E**, **0G**, **0I**, and **0J**, a greater effect of the substituent on the emission properties was observed. In a nonpolar solvent (toluene), **0E**, **0G**, **0I**, and **0J** more closely resemble anthracene, pyrene, and perylene emission profiles. With increasing solvent polarity, the emission maximum of these molecules shifts toward the red, and the bands become unstructured. Therefore, we can consider the formation of intramolecular charge transfer (^{1}ICT) from toluene to DMSO. Compounds dissolved in methanol again present a blue-shifted emission band in the region of the ^{1}LE character. This phenomenon is known for this type of compound.[104] Analyzing the entire group of compounds, significant solvatochromism was observed only for **0G** and **0I** (above 30 nm). To further investigate the excited-state properties of **0G** and **0I**, the Lippert–Mataga solvatochromic model was adopted. The spectra (Fig. S15) show that both compounds exhibit vibronic fine structure in low-polarity solvents. Subsequently, these spectra exhibited a smooth, gradually broadening character, accompanied by a bathochromic shift of more than

30 nm with increasing solvent polarity. This indicates the typical nature of the ICT effect.[98] **0G** and **0I** exhibit a two-section linear relationship with different slopes in low- and high-polarity solvents. The slope of the line in the Lippert–Mataga plot indicates the compound's sensitivity to solvent polarity. This sensitivity indicates a large change in the dipole moment $\Delta\mu$, upon excitation from the ground to the excited state.[105] From the slope of the line, it can be concluded that compound **0G** exhibits a larger change in dipole moment upon excitation than compound **0I**. Fig. S15 and Table S2 show the linear Lippert–Mataga plots with slope values of 6627, 12 119, 4909, and 11 611 cm^{-1} for **0G** and **0I** in low- and high-polarity solvents, respectively. The determined dipole moments in low-polarity solvents were 11.5 D and 9.9 D for **0G** and **0I**, respectively. This can be attributed to an LE-dominated excited state. Moving to the high-polarity region, the dipole moment increases, being 15.5 D for **0G** and 15.2 D for **0I**. This suggests a CT-dominated excited state.[98] Due to the two-component nature of the dipole moment, it can be assumed that these compounds exhibit a mixed state character referred to as HLCT.[98] The analysis of natural transition orbitals (NTO) confirms the HLCT character of the discussed derivatives. As expected, compound **0A** exhibits the greatest blueshift, while **0E** and **0J** show the greatest redshift. The entire group of compounds exhibited high fluorescence quantum yields ranging from 0.08 to 0.56. Furthermore, the effect of argon on QY values was checked. As expected, passing a stream of inert gas (argon) through the test solution increased fluorescence quantum yield.

Solid-state emission measurements were performed for the entire **0A–0J** series (Fig. S16). Emission maxima were in the range from 427 nm to 548 nm. The largest bathochromic shift was observed for compound **0J**. Compared to hexane, red shifts of 16–66 nm were observed in the emission bands. Interestingly, for compounds with a more planar character, the red shift was larger than for non-planar structures. This is because the planarity of the molecules may favor the formation of an intermolecular π–π arrangement, resulting in a large shift in the emission maximum between solution and the solid.[106]

Photoluminescence behavior in the aggregate state was studied for the entire group of compounds (Fig. S13 and S17). Measurements were made by adding various percentages of water to solutions prepared in THF. Gradual aggregation into nanoparticles was observed due to hydrophobic interactions in the presence of water. This inhibits the vibrational rotation of the molecules, and the nonradiative process is significantly suppressed, allowing for a significant increase in emission intensity. For all compounds, a mild increase in emission intensity was observed upon addition of water ($f_w \leq 70$). Interestingly, the maximum photoluminescence intensity for most compounds was observed at 70% water fraction, not at the highest water fraction in the mixture solution. With more than 70% water, a drastic quenching of emissions occurred. This observation can be attributed to a change in the packing order of the aggregates from the crystalline to the amorphous state, or may be due to the solubility of the derivatives in high-water THF/water mixtures.[107]

Photoluminescence and electroluminescent properties

To evaluate the solid-state emission properties of the phenanthro[9,10-*d*]imidazole derivatives **0A–0J**, photoluminescence studies were performed in two representative host matrices, zeonex and CBP – Fig. 6. These environments were selected as a low-polarity inert matrix and a standard OLED host, respectively, allowing the influence of the host on emission energy and radiative efficiency to be assessed. Across the series, the emission maxima span from the blue region for the less extended derivatives to the green region for the perylene-substituted compound **0J**. In general, increasing the effective π-conjugation of the C2 substituent leads to a bathochromic shift of the solid-state emission. A clear host effect is observed for all emitters. For all compounds, emission in CBP was slightly red-shifted (by 10–25 nm) relative to zeonex, consistent

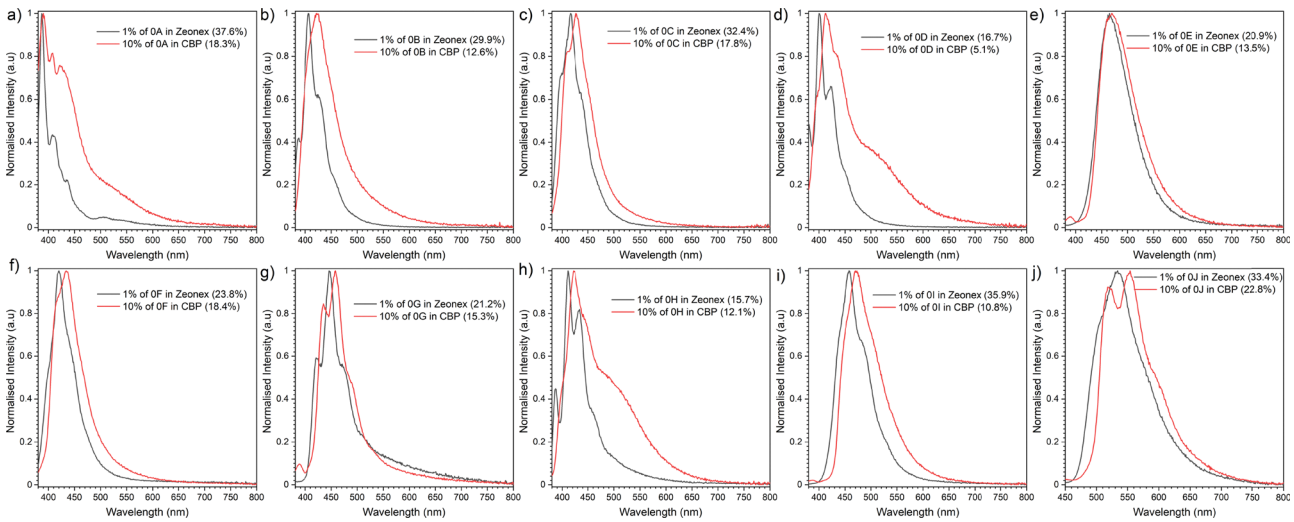

Fig. 6 Photoluminescence spectra and PLQY (%) of emitters in two solid hosts, zeonex and CBP.

with the more polar nature of CBP and possible stabilization of the emissive state. The shorter-conjugated derivatives **0A–0D**, **0F**, and **0H** retain relatively structured blue emission, whereas **0E**, **0G**, **0I**, and **0J** show broader and more substituent-sensitive bands. This behavior is consistent with a greater contribution of the aromatic substituent to the emissive excited state for the latter group, in agreement with the solvatochromic and NTO analyses. Interestingly, the PLQY values were consistently higher in zeonex than in CBP for all derivatives. In zeonex, PLQY ranged from 0.16 (**0H**) to 0.38 (**0A**), whereas in CBP it decreased to 0.5–0.23, depending on the molecule. These results reflect two separate host effects. The red shift observed in CBP is mainly a polarity-related spectral effect, caused by stabilization of the emissive state in the more polar host. The lower PLQY in CBP, however, is treated as an efficiency loss related to enhanced non-radiative decay pathways, while the rigid and nonpolar zeonex matrix better suppresses vibrational relaxation and supports higher radiative efficiency. Among the series, compounds **0A**, **0I**, and **0J** exhibited the highest quantum yields (PLQY = 0.38, 0.36, 0.33 in zeonex, respectively), highlighting their favorable balance between conjugation and rigidity. Notably, **0A** – bearing the smallest aromatic substituent – retains a deep-blue emission with relatively high PLQY, making it an efficient blue fluorescent emitter. In contrast, **0J** shows high PLQY even in the green region, reflecting efficient π-delocalization and minimal nonradiative loss despite its extended structure. At the same time, because only two host matrices were examined and no dedicated morphology studies were performed, host–guest interactions, subtle aggregation effects, or nanoscale phase separation cannot be rigorously excluded. Therefore, the host dependence is discussed here on the basis of the observed spectroscopic trends rather than direct structural proof.

Gated prompt/delayed emission measurements in CBP at 10 K and 300 K indicate that some compounds exhibit a weak delayed component – Fig. 7. However, the present dataset does not allow an unambiguous mechanistic assignment. Therefore, we do not assign this behavior specifically to TADF or TTA and discuss it more conservatively as triplet-related delayed emission. At 10 K, the long-delay spectra are red-shifted relative to the prompt fluorescence, which is consistent with triplet-related emission and allows estimation of the singlet and triplet energies. The resulting ΔE_{ST} values span a relatively broad range

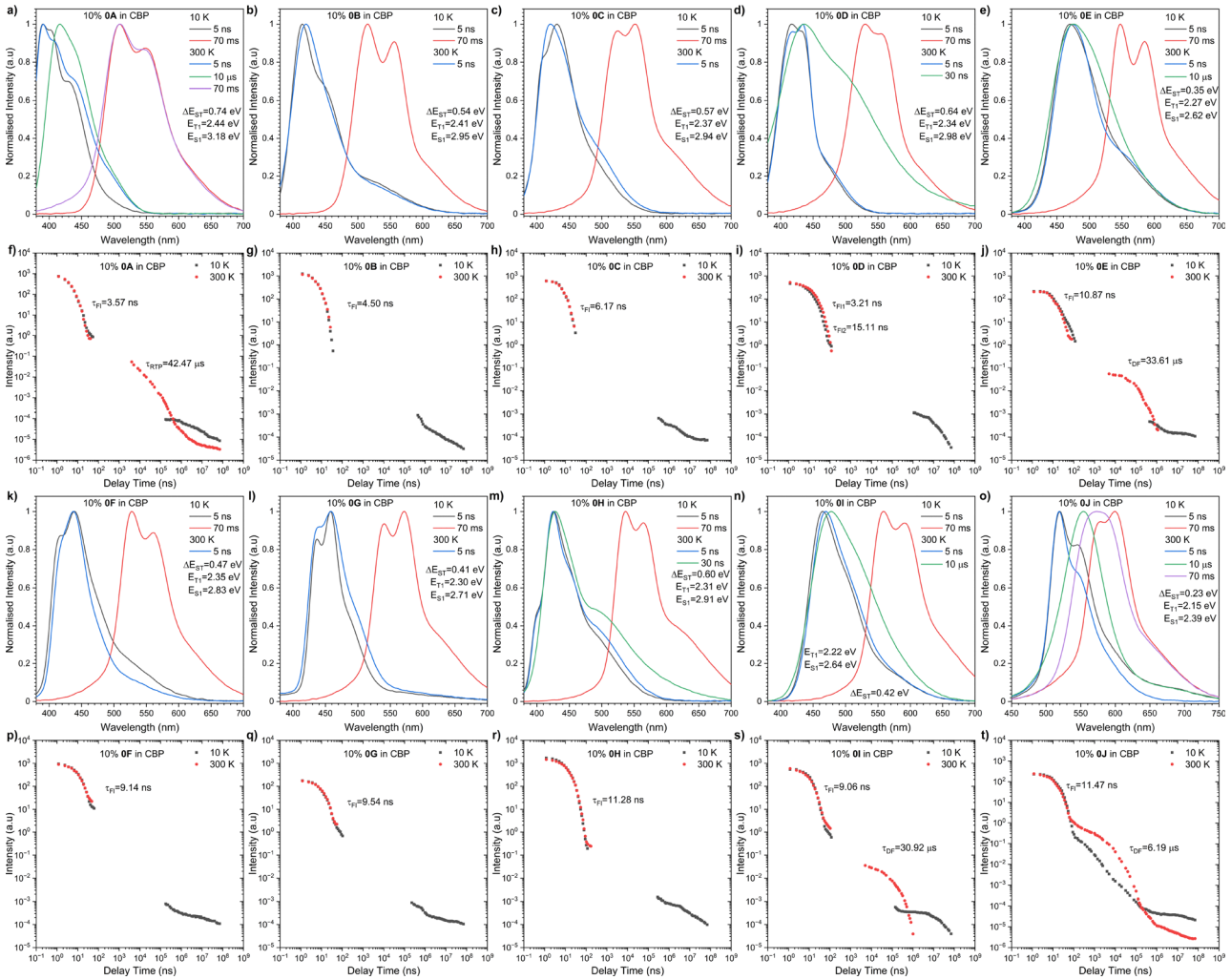

Fig. 7 Time-resolved photoluminescence study of compound **0A–0J** in CBP at 10 K and 300 K.

across the series and remain comparatively large for most compounds. For the best-performing OLED emitters, ΔE_{ST} is *ca.* 0.35 eV for **0E**, 0.42 eV for **0I**, and 0.23 eV for **0J**. These values do not support efficient classical TADF for the full series. Overall, the most probable dominant emission pathway is prompt fluorescence from the singlet excited state, while the observed delayed emission represents only a minor triplet-assisted contribution; therefore, efficient TADF is unlikely to be the main mechanism in this series.

OLED devices incorporating the new emitters were fabricated using the following architecture: ITO/PEDOT:PSS (40 nm)/PVK (10 nm)/CBP:**0A–0J** (10 wt%, 30 nm)/TmPyPB (40 nm)/LiF (1 nm)/Al (100 nm) – Fig. 8a. PEDOT:PSS served as the hole injection/transport layer, PVK acted as an electron-blocking layer, CBP as the emissive host, and TmPyPB as the electron-transporting layer. The energy level alignment is consistent with feasible charge injection in the multilayer device architecture. All devices displayed bright electroluminescence with emission wavelengths corresponding to their PL in CBP (Fig. 6). The emission color evolved from deep-blue for **0A** (λ_{EL} = 402 nm) to green for **0J** (λ_{EL} = 515–566 nm), consistent with the optical gap variation. The CIE coordinates ranged from (0.1645, 0.0849) for **0C** to (0.3802, 0.5642) for **0J** – Fig. 8b. The photoluminescence and OLED parameters are summarized in Table 6. For each emitter formulation, several device pixels were fabricated, and the values discussed here correspond to a representative device pixel. Since the present work is intended as a comparative structure–property study, a full statistical reproducibility analysis was outside the scope of this manuscript. The best overall device performance was obtained for **0J**, which reached EQE_{max} = 4.29% and L_{max} = 8962 cd m^{-2}. Assuming an optical outcoupling factor of 20–30%, which is a typical literature range for conventional planar OLEDs without additional light-extraction structures, the EQE of 4.29% corresponds to an apparent internal quantum efficiency of *ca.* 14–21%; this value should be treated only as an approximate estimate.[108–110] This value is somewhat higher than the simple singlet-only expectation based on 25% singlet formation and the measured PLQY in CBP, which is consistent with a limited additional triplet-related contribution, although the present data do not allow us to determine whether it arises from TTA, weak RISC, or another triplet-mediated process. Additional uncertainty may also arise from differences in actual outcoupling, emitter orientation, and the difference between separately measured film PLQY and the real emissive layer in the device. Good efficiencies were also obtained for **0A** and **0E**, whereas **0D** was the least efficient emitter in the series. Overall, the better-performing devices combine favorable solid-state PLQY with more favorable energetic parameters for charge injection and transport, particularly in the case of the more

Table 6 Photoluminescence and electroluminescent properties for compounds **0A–0J**

		Photoluminescence		Device		
Compound	Host	λ_{em} [nm]	PLQY	L_{max} [cd m^{-2}]	EQE [%]	CIE [x; y]
0A	Zeonex	388	0.38	—	—	—
	CBP	402	0.18	6963	2.67	0.1925; 0.1633
0B	Zeonex	407	0.30	—	—	—
	CBP	420	0.13	3578	1.03	0.1819; 0.1311
0C	Zeonex	417	0.32	—	—	—
	CBP	430	0.18	1963	1.20	0.1645; 0.0849
0D	Zeonex	402	0.17	—	—	—
	CBP	421	0.05	3000	0.37	0.2035; 0.2037
0E	Zeonex	468	0.21	—	—	—
	CBP	477	0.13	4221	2.62	0.1828; 0.2634
0F	Zeonex	421	0.24	—	—	—
	CBP	435	0.18	5192	1.23	0.1670; 0.1017
0G	Zeonex	449	0.21	—	—	—
	CBP	459	0.15	3620	1.11	0.1714; 0.1417
0H	Zeonex	413	0.16	—	—	—
	CBP	432	0.12	3277	0.92	0.2002; 0.2176
0I	Zeonex	457	0.36	—	—	—
	CBP	475	0.11	4190	2.12	0.1794; 0.2668
0J	Zeonex	539	0.33	—	—	—
	CBP	566	0.23	8962	4.29	0.3802; 0.5643

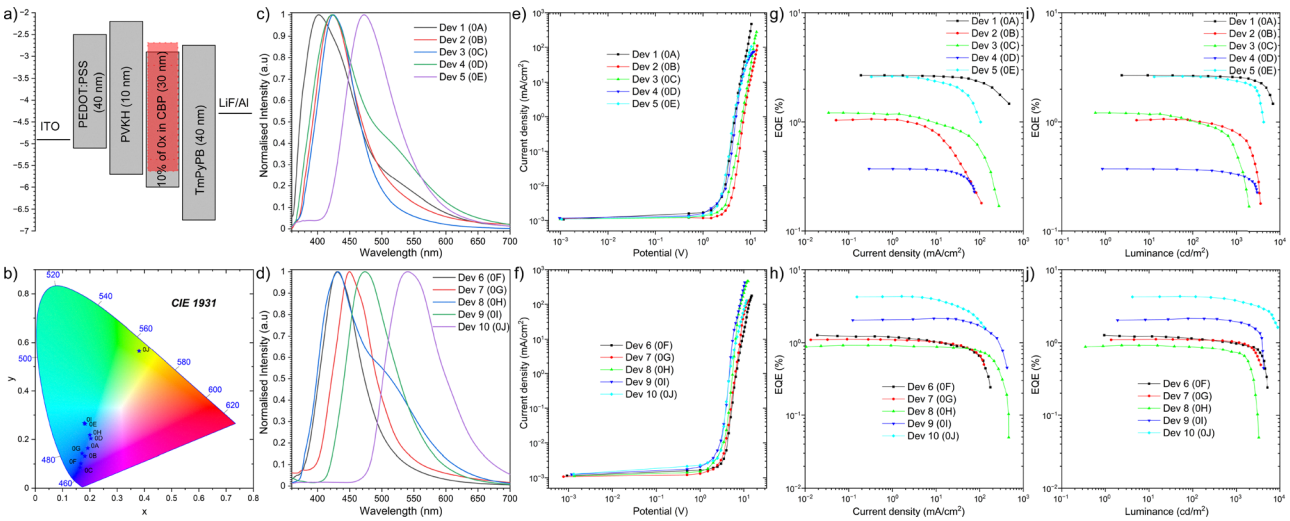

Fig. 8 (a) OLED architecture; (b) chromaticity diagram; (c) and (d) electroluminescence spectra; (e) and (f) current density-bias characteristic; (g) and (h) EQE – current density; (i) and (j) EQE – luminance characteristics.

extended substituents **0E**, **0I**, and **0J**. Although the emitters showing a more noticeable delayed contribution also tend to give higher EQE values, the present measurements are insufficient to identify a unique exciton-harvesting mechanism. Accordingly, the OLED results are discussed here primarily in terms of empirical structure–property relationships rather than definitive excited-state kinetics.

Nevertheless, a weak delayed component is observed for selected compounds at room temperature. In the cases of **0E** and **0I**, the delayed spectra remain close to the prompt fluorescence, which is consistent with delayed emission originating from the same or a closely related emissive state. For **0J**, the delayed emission is more red-shifted, indicating a stronger contribution from a lower-energy triplet-related state. These observations suggest that triplet states may participate in the emissive process. Possible explanations include triplet–triplet annihilation (TTA), weak reverse intersystem crossing (RISC)-assisted delayed fluorescence, or an RTP-like contribution.[111,112] From the device perspective, TTA or weak RISC could provide limited additional harvesting of triplet excitons and thus help explain why the measured EQE is somewhat higher than a simple fluorescence-only estimate based only on PLQY and 25% singlet formation.[112] However, because the delayed component is weak and the corresponding efficiency enhancement is only moderate, the present data suggest at most a limited triplet-assisted contribution rather than efficient TADF as a dominant mechanism.[112] An RTP-like pathway may also contribute to delayed emission, particularly if the delayed spectrum is shifted relative to the prompt one, but such a contribution would not necessarily lead to a pronounced EQE increase.[111] Therefore, the present results support only a cautious assignment to weak triplet-related delayed emission, without distinguishing unambiguously between TTA, weak RISC, and RTP.

Current density–voltage (*J*–*V*) measurements (Fig. 8e–h) revealed non-linear characteristics, confirming efficient carrier injection through the multilayer stack. The turn-on voltages ranged between 3.2 and 4.1 V, depending on the emitter.

The external quantum efficiencies (EQE) followed the expected photophysical trends:

- **0A**: 2.67% (deep-blue, 402 nm);
- **0D**: 0.37% (blue, 421 nm);
- **0E**: 2.62% (cyan, 477 nm);
- **0I**: 2.12% (blue-green, 475 nm);
- **0J**: 4.29% (green, 515–566 nm) – the highest across the series.

The maximum luminance reached 8960 cd m^{-2} for **0J** and 1963 cd m^{-2} for **0C** (Fig. 8i and j). The efficiency roll-off was less pronounced for **0E**, **0I**, and **0J** than for the least efficient emitters in the series. The structure–property relationship between the PL and EL behaviors reveals that the compounds exhibiting partial delayed fluorescence in zeonex also display higher EQE in OLED devices. This correlation suggests that triplet-related processes may contribute to the observed performance, but the present data do not allow a definitive mechanistic assignment.

Conclusions

In the conducted studies, ten phenanthro[9,10-*d*]imidazole derivatives (**0A–0J**) were obtained *via* condensation reactions. The compounds considered differed in their aromatic substituents at the C2 position. They were classified as follows, taking into account the increasing number of aromatic rings and the manner of their attachment to the phenanthro[9,10-*d*]imidazole core: phenyl (**0A**), biphenyl-1-yl (**0B**), naphthalen-1-yl (**0C**), naphthalen-2-yl (**0D**), anthracen-9-yl (**0E**), phenanthren-9-yl (**0F**), anthracen-2-yl (**0G**), triphenylen-2-yl (**0H**), pyren-1-yl (**0I**). All derivatives were purified by crystallization in methanol, and NMR and HRMS confirmed their structures. In terms of thermal properties, all phenanthro[9,10-*d*]imidazole derivatives exhibit thermal stability above 290 °C. However, this parameter does not increase exponentially with the increase in the number of aromatic rings in the substituent. It is primarily related to their arrangement and the position of attachment to the phenanthro[9,10-*d*]imidazole core. Electrochemical studies showed that the oxidation process occurred most readily for the **0E**, **0G**, **0I**, and **0J** molecules. The remaining derivatives were oxidized above 0.5 V. The reduction process occurred at potentials below −2 V. Interestingly, the **0G** compound was most readily reduced (−1.89 V). In this case, the substituent at the C2 position had a significant impact on the reduction. In systems with a longer conjugated system, reduction occurs much more easily (**0E**, **0G**, **0I**). A special case is the **0J** derivative, for which reduction occurs most readily (−1.89 V), and the process is thermodynamically reversible. DFT calculations revealed nonplanar geometry for most of the molecules. This leads to less delocalization of π electrons between the aromatic substituent and the 1*H*-phenanthro[9,10-*d*]imidazole core in the ground state. The exceptions are **0A**, **0D**, **0G**, and **0H**. Furthermore, the molecules under consideration do not exhibit well-resolved distributions of the highest occupied molecular orbital (HOMO) and lowest unoccupied molecular orbital (LUMO). The calculated energy gaps resulting from the difference between IP and EA range from 2.57 eV to 3.86 eV. Simulated absorption spectra indicate that the lowest-energy absorption bands correspond to HOMO → LUMO transitions. Optical studies have shown that absorption bands in the 300–350 nm range are associated with π–π* transitions originating from the 1*H*-phenanthro[9,10-*d*]imidazole core. The absorption spectra of **0A–0D**, **0F**, and **0H** are relatively insensitive to the attached aromatic group (at the C2 position) over the entire spectral range. In the cases of **0E**, **0G**, and **0J**, bands appearing above 350 nm can be observed, exhibiting spectral features typical of anthracene and perylene absorption. The emission spectra of the **0A–0D**, **0H**, and **0F** derivatives indicate emission from a locally excited singlet emission state (^{1}LE). In compounds **0E**, **0G**, **0I**, and **0J**, a greater effect of the substituent on the emission properties was observed. In a nonpolar solvent (toluene), **0E**, **0G**, **0I**, and **0J** more closely resemble the emission profiles of anthracene, pyrene, and perylene. As the solvent polarity increases, the emission maximum of these molecules shifts toward the red, and the bands become less structured.

Therefore, we can consider the formation of ^{1}ICT from toluene to DMSO. The photophysical and electroluminescent studies demonstrate that the emission color and device performance of phenanthro[9,10-*d*]imidazole derivatives can be effectively tuned by varying the aromatic substituent at the C2 position. Zeonex provides a more favorable environment for radiative emission, whereas CBP enables practical OLED fabrication but leads to lower PLQY values. The best overall device performance was obtained for the perylene derivative **0J**, while **0E** and **0I** were also among the more promising emitters in the series. Importantly, the present results show that simply increasing the number of aromatic rings is not sufficient to improve performance; the arrangement of the rings, the position of attachment, and the resulting torsion angle are equally important. These findings provide a useful design guideline for further development of phenanthroimidazole-based fluorescent emitters.

In summary, the conducted studies have shown that increasing the number of aromatic rings in the C2 substituent of phenanthro[9,10-*d*]imidazole derivatives does not always improve their physicochemical properties or the parameters of the constructed OLEDs. The arrangement of the aromatic rings in the substituent and the position of their attachment to the molecular core are crucial. The substituent torsion angle is also important, as it influences the properties of the compounds under consideration. The compounds exhibiting the best parameters in the test OLED devices were **0E**, **0I**, and **0J**. All of these derivatives contained an extended aromatic system in the C2 substituent, based on anthracene (**0E**), pyrene (**0I**), or perylene (**0J**). Furthermore, the compounds under discussion were characterized by a mild torsion angle of the substituent. Therefore, based on the studies conducted, the best substituents for further modification of phenanthro[9,10-*d*]imidazole derivatives are anthracene, pyrene, and perylene.

Conflicts of interest

The authors declare no competing financial interest.

Data availability

The supporting data has been provided as part of the supplementary information (SI). Supplementary information: Tables S1 and S2, NMR spectra and further experimental details. See DOI: https://doi.org/10.1039/d6tc00518g.

Acknowledgements

Calculations have been carried out using resources provided by Wroclaw Centre for Networking and Supercomputing (https://wcss.pl). Grant No. 18. PD and JL acknowledge that research was co-funded by the project Horizon Europe GHOST (101182946) and by the Polish Ministry of Education and Science under the program 'Internationally Co-Financed Projects' (W115/HE/2024). This work was supported by the Polish National Science Center, Poland (2022/45/B/ST5/03712). This work was co-funded by the project: ''jUŚt transition – Potencjał Uniwersytetu Śląskiego podstawą Sprawiedliwej Transformacji regionu'' (FESL.10.25- IZ.01.0369/23-003). The project is implemented under the European Funds for Silesia 2021–2027. Program co-financed by the Just Transition.

Notes and references

1 C. W. Tang and S. A. VanSlyke, *Appl. Phys. Lett.*, 1987, **51**, 913–915.
2 K. T. Kamtekar, A. P. Monkman and M. R. Bryce, *Adv. Mater.*, 2010, **22**, 572–582.
3 Z. Cheng, C. Du, S. Ge, Y. Wang, F. Liu, Y. Chang, Y. Lv and P. Lu, *Chem. Eng. J.*, 2023, **474**, 145867.
4 S.-J. Zou, Y. Shen, F.-M. Xie, J.-D. Chen, Y.-Q. Li and J.-X. Tang, *Mater. Chem. Front.*, 2020, **4**, 788–820.
5 S. Xiao, Y. Gao, R. Wang, H. Liu, W. Li, C. Zhou, S. Xue, S.-T. Zhang, B. Yang and Y. Ma, *Chem. Eng. J.*, 2022, **440**, 135911.
6 S. Ge, C. Du, Z. Cheng, Y. Wang, Z. Feng, Z. Yan, Y. Hu and P. Lu, *Chem. Eng. J.*, 2024, **489**, 151314.
7 R. R. Søndergaard, M. Hösel and F. C. Krebs, *J. Polym. Sci., Part B:Polym. Phys.*, 2013, **51**, 16–34.
8 C. W. Lee and J. Y. Lee, *Adv. Mater.*, 2013, **25**, 596–600.
9 M. Colella, P. Pander and A. P. Monkman, *Org. Electron.*, 2018, **62**, 168–173.
10 H.-W. Chen, J.-H. Lee, B.-Y. Lin, S. Chen and S.-T. Wu, *Light: Sci. Appl.*, 2018, **7**, 17168.
11 B. Pashaei, S. Karimi, H. Shahroosvand, P. Abbasi, M. Pilkington, A. Bartolotta, E. Fresta, J. Fernandez-Cestau, R. D. Costa and F. Bonaccorso, *Chem. Soc. Rev.*, 2019, **48**, 5033–5139.
12 G. M. Farinola and R. Ragni, *J. Solid State Light.*, 2015, **2**, 9.
13 D. Kumar, K. R. J. Thomas, C.-C. Lin and J.-H. Jou, *Chem. – Asian J.*, 2013, **8**, 2111–2124.
14 S. Ye, Y. Wang, R. Guo, Q. Zhang, X. Lv, Y. Duan, P. Leng, S. Sun and L. Wang, *Chem. Eng. J.*, 2020, **393**, 124694.
15 J. Y. Woo, M.-H. Park, S.-H. Jeong, Y.-H. Kim, B. Kim, T.-W. Lee and T.-H. Han, *Adv. Mater.*, 2023, **35**, 2207454.
16 H. Wu, Y.-Z. Shi, M.-Y. Li, X.-C. Fan, H. Wang, T.-Y. Zhang, J.-X. Chen, J. Yu and K. Wang, *Chem. Eng. J.*, 2025, **516**, 164225.
17 A. Kraft, A. C. Grimsdale and A. B. Holmes, *Angew. Chem., Int. Ed.*, 1998, **37**, 402–428.
18 Y. Liu, L. Hua, S. Yan and Z. Ren, *Nano Energy*, 2020, **73**, 104800.
19 J.-M. Teng, D.-W. Zhang, Y.-F. Wang and C.-F. Chen, *ACS Appl. Mater. Interfaces*, 2022, **14**, 1578–1586.
20 M. Li, L. Hua, J. Liu and Z. Ren, *Mater. Chem. Front.*, 2023, **7**, 6141–6153.
21 T. Wang, J. Dong, M. Chen, P. Tao, B. Zhang, Y.-J. Pu, C. Yang and W.-Y. Wong, *Chem. Eng. J.*, 2025, **517**, 164120.
22 H. Zhuang, A. Zhu, J. Jiang, W. Shi, H. Zhou, S. Hu, W. Bian, M. Li and X. Ban, *Chem. Eng. J.*, 2025, **519**, 164942.

23 D. Ma, C. Zhang, Y. Qiu and L. Duan, *Org. Electron.*, 2016, **39**, 16–24.
24 P. Tao, W.-L. Li, J. Zhang, S. Guo, Q. Zhao, H. Wang, B. Wei, S.-J. Liu, X.-H. Zhou, Q. Yu, B.-S. Xu and W. Huang, *Adv. Funct. Mater.*, 2016, **26**, 881–894.
25 C. Bizzarri, E. Spuling, D. M. Knoll, D. Volz and S. Bräse, *Coord. Chem. Rev.*, 2018, **373**, 49–82.
26 K. Xu, J. Zheng, F. Zhan, W. Lou, X. Fang, Q. Chen, H. Guo, W. Chen, Y.-F. Yang, Y. She and G. Li, *Chem. Eng. J.*, 2025, **506**, 159948.
27 F. Zhan, K. Xu, J. Zheng, Q. Chen, G. Shen, J. Dai, Q. Feng, H. Guo, S. Liu, J. Ying, J. Tong, W. Lou, Y.-F. Yang, S. Chen, Y. She and G. Li, *Chem. Eng. J.*, 2025, **524**, 169759.
28 F. Zhan, T.-S. Zhang, J. Chen, K. Xu, J. Tong, Y.-F. Yang, Y. She and G. Li, *Chem. Eng. J.*, 2025, **521**, 166619.
29 L. Duan, L. Hou, T.-W. Lee, J. Qiao, D. Zhang, G. Dong, L. Wang and Y. Qiu, *J. Mater. Chem.*, 2010, **20**, 6392–6407.
30 S. K. Jeon, H.-J. Park and J. Y. Lee, *J. Mater. Chem. C*, 2018, **6**, 6778–6783.
31 H. Peng, Z. Wei, L. Wu and X. Li, *Opt. Mater.*, 2020, **101**, 109726.
32 A. Sharma, K. R. J. Thomas, M. R. Nagar and J.-H. Jou, *Mater. Adv.*, 2021, **2**, 6326–6338.
33 S. Xu, X. Du, X. Yang, H. Hang, J. Xi, G. Zhou and Y. Sun, *Org. Electron.*, 2025, **137**, 107182.
34 M. Li, Z. Li, X. Peng, D. Liu, C. Zijian, W. Xie, L. Kunkun and S. Su, *Angew. Chem., Int. Ed.*, 2025, **64**, e202420474.
35 H.-S. Liao, B.-Y. Wang, D. Chen, J.-H. Liu, R.-T. Zhao, H. Chi, Y.-L. Lv, B. Zhao and X. Li, *Chem. Eng. J.*, 2025, **520**, 166017.
36 X. Yang, X. Xu and G. Zhou, *J. Mater. Chem. C*, 2015, **3**, 913–944.
37 Z. Wang, B. Zhang, Y. Chen, J. Pei, Q. Jia, C. Hao, X. Lei and D. Wang, *J. Mater. Chem. C*, 2025, **13**, 4461–4471.
38 J. Tagare and S. Vaidyanathan, *J. Mater. Chem. C*, 2018, **6**, 10138–10173.
39 J. Jayabharathi, S. Panimozhi and V. Thanikachalam, *Sci. Rep.*, 2019, **9**, 17555.
40 L. Peng, Y. Huo, L. Hua, J. Lv, Y. Liu, S. Ying and S. Yan, *J. Mater. Chem. C*, 2022, **10**, 9621–9627.
41 Y. Jia, S. Wu, Y. Zhang, S. Fan, X. Zhao, H. Liu, X. Dong, S. Wang and X. Li, *Org. Electron.*, 2019, **69**, 289–296.
42 W.-C. Chen, Y. Yuan, Y. Xiong, A. L. Rogach, Q.-X. Tong and C.-S. Lee, *ACS Appl. Mater. Interfaces*, 2017, **9**, 26268–26278.
43 Z.-Y. Wang, B. Liu, J.-W. Zhao, G.-L. Ruan, S.-L. Tao and Q.-X. Tong, *Org. Electron.*, 2018, **52**, 89–97.
44 S. Chen, Y. Wu, Y. Zhao and D. Fang, *RSC Adv.*, 2015, **5**, 72009–72018.
45 J. Tagare, R. Boddula, S. S. Sudheendran, D. K. Dubey, J.-H. Jou, S. Patel and S. Vaidyanathan, *J. Mater. Chem. C*, 2020, **8**, 16834–16844.
46 J. Jayabharathi, A. Prabhakaran, V. Thanikachalam and P. Jeeva, *New J. Chem.*, 2016, **40**, 8768–8777.
47 V. Thanikachalam, E. Sarojpurani, J. Jayabharathi and P. Jeeva, *New J. Chem.*, 2017, **41**, 2443–2457.
48 X. Tang, H. Liu, F. Liu, X. He, X. Xu, J. Chen, Q. Peng and P. Lu, *Chem. – Asian J.*, 2021, **16**, 1942–1948.
49 J. Tagare, R. A. K. Yadav, S. S. Swayamprabha, D. K. Dubey, J.-H. Jou and S. Vaidyanathan, *J. Mater. Chem. C*, 2021, **9**, 4935–4947.
50 Z. Li, N. Xie, Y. Xu, C. Li, X. Mu and Y. Wang, *Org. Mater.*, 2020, **02**, 011–019.
51 F. Liu, Y. Tan, H. Liu, X. Tang, L. Gao, C. Du, J. Min, H. Jin and P. Lu, *J. Mater. Chem. C*, 2020, **8**, 6883–6890.
52 J. Xin, Z. Li, Y. Liu, D. Liu, F. Zhu, Y. Wang and D. Yan, *J. Mater. Chem. C*, 2020, **8**, 10185–10190.
53 W. Cao, A. Abdurahman, P. Zheng, M. Zhang and F. Li, *J. Mater. Chem. C*, 2021, **9**, 6873–6879.
54 S. S. Reddy, V. G. Sree, K. Gunasekar, W. Cho, Y. Gal, M. Song, J. Kang and S. Jin, *Adv. Opt. Mater.*, 2016, **4**, 1236–1246.
55 J. Jayabharathi, S. Sivaraj, V. Thanikachalam and J. Anudeebhana, *J. Mater. Chem. C*, 2021, **9**, 10334–10346.
56 D.-H. Wang, J.-F. Yao, H.-Z. Li, G.-Z. Li, F.-M. Xie, Y.-Q. Li, Y.-Y. Hu, J.-X. Tang and X. Zhao, *New J. Chem.*, 2023, **47**, 3026–3036.
57 C. Li, J. Wei, X. Song, K. Ye, H. Zhang, J. Zhang and Y. Wang, *J. Mater. Chem. C*, 2016, **4**, 7013–7019.
58 P. Keerthika, A. Kumar, A. Selvaganesan, J. Moon, V. Nutalapati, J. Y. Lee and R. K. Konidena, *J. Mater. Chem. C*, 2025, **13**, 20540–20548.
59 B. Wang, G. Mu, J. Tan, Z. Lei, J. Jin and L. Wang, *J. Mater. Chem. C*, 2015, **3**, 7709–7719.
60 J. Huo, C. Gao, Y. Cao, H. Shi and B. Z. Tang, *J. Mater. Chem. C*, 2023, **11**, 4456–4465.
61 C. Du, T. Lu, Z. Cheng, Y. Chang, H. Liu, J. Wang, L. Wan, Y. Lv and P. Lu, *J. Mater. Chem. C*, 2022, **10**, 14186–14193.
62 P. Chasing, J. Kumsampao, P. Janthakit, P. Nalaoh, T. Loythaworn, W. Waengdongbung, P. Wongkaew, T. Sudyoadsuk and V. Promarak, *J. Mater. Chem. C*, 2023, **11**, 14776–14786.
63 T. Jairam and W. P. Hong, *J. Mater. Chem. C*, 2022, **10**, 16173–16217.
64 C. Liu, J. Li, X. Man, H. Liu, X. Sun, F. Liu and P. Lu, *Chem. – Asian J.*, 2019, **14**, 821–827.
65 F. Zhang, W. Li, D. Wei, X. Wei, Z. Li, S. Zhang, S. Li, B. Wei, G. Cao and B. Zhai, *RSC Adv.*, 2016, **6**, 60264–60270.
66 C. Kaiyasuan, P. Chasing, P. Nalaoh, P. Wongkaew, T. Sudyoadsuk, K. Kongpatpanich and V. Promarak, *Chem. – Asian J.*, 2021, **16**, 2328–2337.
67 M. Zurnacı, İ. Şener, M. Gür and N. Şener, *Luminescence*, 2023, **38**, 1690–1701.
68 W. Liu, X. Sun, H. Zhou, Y. Chen, L. Zhang, B. Wei, W. Shi, Z. Zhang and J. Huang, *Dyes Pigm.*, 2026, **245**, 113280.
69 Y. Huang, J. Lou, B. Li, H. Zhang, Y. Chen, X. He, X. Qiao, B. Z. Tang and Z. Wang, *Chem. Eng. J.*, 2025, **505**, 159034.
70 L. Peng, J. Lv, S. Xiao, Y. Huo, Y. Liu, D. Ma, S. Ying and S. Yan, *Chem. Eng. J.*, 2022, **450**, 138339.
71 G. Yang, Y. Ran, Y. Wu, M. Chen, Z. Bin and J. You, *Aggregate*, 2023, **4**, e199.

72 I. De Moraes, S. Scholz, M. Hermenau, M. Tietze, T. Schwab, S. Lenk, M. Gather and K. Leo, *Org. Electron.*, 2015, **26**, 158–163.
73 P. Tyagi, R. Srivastava, L. Giri, S. Tuli and C. Lee, *Synth. Met.*, 2015, 216.
74 S. Sudheendran Swayamprabha, D. K. Dubey, Shahnawaz, R. A. K. Yadav, M. R. Nagar, A. Sharma, F. Tung and J. Jou, *Adv. Sci.*, 2020, **8**, 2002254.
75 B. B. Meer, D. Sharma, S. Tak, G. G. Bisen, M. D. Shirsat, K. G. Girija and S. S. Ghosh, *RSC Adv.*, 2023, **13**, 33668–33674.
76 P. Bujak, I. Kulszewicz-Bajer, M. Zagorska, V. Maurel, I. Wielgus and A. Pron, *Chem. Soc. Rev.*, 2013, **42**, 8895–8999.
77 P. Keerthika, A. Kumar, A. Maruthapillai, V. Nutalapati and R. K. Konidena, *J. Photochem. Photobiol., C*, 2025, **63**, 100698.
78 Z. Wang, P. Lu, S. Chen, Z. Gao, F. Shen, W. Zhang, Y. Xu, H. S. Kwok and Y. Ma, *J. Mater. Chem.*, 2011, **21**, 5451–5456.
79 S. Kula, A. Szlapa-Kula, S. Kotowicz, M. Filapek, K. Bujak, M. Siwy, H. Janeczek, S. Maćkowski and E. Schab-Balcerzak, *Dyes Pigm.*, 2018, **159**, 646–654.
80 S. Kula, Ł. Kaźmierski, M. Filapek and P. Krawczyk, *J. Mol. Struct.*, 2023, **1281**, 135151.
81 C. Adamo and V. Barone, *J. Chem. Phys.*, 1999, **110**, 6158–6170.
82 M. Ernzerhof and G. E. Scuseria, *J. Chem. Phys.*, 1999, **110**, 5029–5036.
83 F. Weigend and R. Ahlrichs, *Phys. Chem. Chem. Phys.*, 2005, **7**, 3297–3305.
84 D. Rappoport and F. Furche, *J. Chem. Phys.*, 2010, **133**, 134105.
85 D. Andrae, U. Häußermann, M. Dolg, H. Stoll and H. Preuß, *Theor. Chim. Acta*, 1990, **77**, 123–141.
86 B. P. Pritchard, D. Altarawy, B. Didier, T. D. Gibson and T. L. Windus, *J. Chem. Inf. Model.*, 2019, **59**, 4814–4820.
87 D. Feller, *J. Comput. Chem.*, 1996, **17**, 1571–1586.
88 K. L. Schuchardt, B. T. Didier, T. Elsethagen, L. Sun, V. Gurumoorthi, J. Chase, J. Li and T. L. Windus, *J. Chem. Inf. Model.*, 2007, **47**, 1045–1052.
89 A. D. Becke, *J. Chem. Phys.*, 1996, **104**, 1040–1046.
90 S. Miertuš, E. Scrocco and J. Tomasi, *Chem. Phys.*, 1981, **55**, 117–129.
91 A. Szlapa-Kula, M. Małecka and B. Machura, *Dyes Pigm.*, 2020, **180**, 108480.
92 G. Velmurugan, B. K. Ramamoorthi and P. Venuvanalingam, *Phys. Chem. Chem. Phys.*, 2014, **16**, 21157–21171.
93 X.-K. Chen, L.-Y. Zou, A.-M. Ren and J.-X. Fan, *Phys. Chem. Chem. Phys.*, 2011, **13**, 19490–19498.
94 A. Krawiec, M. Filapek and S. Kula, *Materials*, 2026, **19**(1), 55.
95 S. Zhang, W. Li, L. Yao, Y. Pan, F. Shen, R. Xiao, B. Yang and Y. Ma, *Chem. Commun.*, 2013, **49**, 11302–11304.
96 W. Li, G. Dong, H. Wang, J. Liu, J. Chen, Y. Dong and C. Zhang, *J. Mol. Struct.*, 2024, **1307**, 137977.
97 S. Kula, A. Szlapa-Kula, S. Kotowicz, M. Filapek, K. Bujak, M. Siwy, H. Janeczek, S. Maćkowski and E. Schab-Balcerzak, *Dyes Pigm.*, 2018, **159**, 646–654.
98 D.-D. Xie, H.-S. Liao, B.-Y. Wang, D. Chen, H.-J. Chi, Y.-L. Lv, Y. Dong and X. Li, *Chem. – Eur. J.*, 2024, **30**, e202400121.
99 F. C. Krebs and H. Spanggaard, *J. Org. Chem.*, 2002, **67**, 7185–7192.
100 M. S. Subeesh, K. Shanmugasundaram, C. D. Sunesh, Y. S. Won and Y. Choe, *J. Mater. Chem. C*, 2015, **3**, 4683–4687.
101 M. Subeesh, K. Shanmugasundaram, C. D. Sunesh, T. Nguyen and Y. Choe, *J. Phys. Chem. C*, 2015, **119**, 23676–23684.
102 R. Ahmed, A. Ali, M. Ahmad, A. Alsalme, R. Ahmad Khan and F. Ali, *New J. Chem.*, 2020, **44**, 20092–20100.
103 P. Guiglion and M. A. Zwijnenburg, *Phys. Chem. Chem. Phys.*, 2015, **17**, 17854–17863.
104 S. Kula, P. Krawczyk, M. Filapek and A. M. Maroń, *J. Lumin.*, 2021, **233**, 117910.
105 J. Wiefermann, J. M. Kaminski, E. Pankert, D. Hertel, K. Meerholz, C. M. Marian and T. J. J. Müller, *ChemPhotoChem*, 2023, **7**, e202200265.
106 X. Cao, L. Meng, Z. Li, Y. Mao, H. Lan, L. Chen, Y. Fan and T. Yi, *Langmuir*, 2014, **30**, 11753–11760.
107 A. A. Saddik, A. A. K. Mohammed, S. K. Talloj, A. M. K. El-Dean and O. Younis, *RSC Adv.*, 2024, **14**, 6072–6084.
108 Q. Xue and G. Xie, *Adv. Opt. Mater.*, 2021, **9**, 2002204.
109 S.-Y. Kim and J.-J. Kim, *Org. Electron.*, 2010, **11**, 1010–1015.
110 J. Song, H. Lee, E. G. Jeong, K. C. Choi and S. Yoo, *Adv. Mater.*, 2020, **32**, 1907539.
111 S. Hirata, *Appl. Phys. Rev.*, 2022, **9**, 011304.
112 P. Data and Y. Takeda, *Chem. – Asian J.*, 2019, **14**, 1613–1636.

